Collective out-of-plane magnetization reversal in tilted stripe domain systems via a single point of irreversibility

Peter Heinig,[1,2,*] Ruslan Salikhov,[1] Fabian Samad,[1,2] Lorenzo Fallarino,[1,3] Gauravkumar Patel,[1] Attila Kákay,[1] Nikolai S. Kiselev,[4] and Olav Hellwig[1,2,5]

[1]*Institute of Ion Beam Physics and Materials Research, Helmholtz-Zentrum Dresden-Rossendorf, 01328 Dresden, Germany*

[2]*Institute of Physics, Chemnitz University of Technology, 09107 Chemnitz, Germany*

[3]*CIC energiGUNE, Parque Tecnológico de Álava, 01510 Vitoria-Gasteiz, Álava, Spanien*

[4]*Peter Grünberg Institute and Institute for Advanced Simulation, Forschungszentrum Jülich and JARA, 52425 Jülich, Germany*

[5]*Center for Materials, Architectures and Integration of Nanomembranes (MAIN), Chemnitz University of Technology, 09107 Chemnitz, Germany*

(Received 20 November 2023; revised 24 April 2024; accepted 21 June 2024; published 12 July 2024)

Perpendicular magnetic anisotropy thin film systems are well known for their periodic magnetic stripe domain structures. In this study, we focus on investigating the behavior of $[Co(3.0\ nm)/Pt(0.6\ nm)]_X$ multilayers within the transitional regime from preferred in-plane to out-of-plane magnetization orientation. Particularly, we examine the sample with $X = 11$ repetitions, which exhibits a remanent state characterized by a significant presence of both out-of-plane (OOP) and in-plane (IP) magnetization components, here referred to as the "tilted" stripe domain state. Vector vibrating sample magnetometry and magnetic force microscopy are used to investigate this specific sample and its unusual out-of-plane reversal behavior. Through experimental data analysis and micromagnetic simulations of the tilted magnetization system, we identify a single point of irreversibility during an out-of-plane external magnetic field sweep. This behavior is qualitatively similar to the reversal of a Stoner-Wohlfarth particle or of an IP magnetized disk with remanent vortex structure, since both show distinct points of irreversibility as well. Such a collective response to an external field is typically not observed in conventional OOP or IP systems, where the reversal process often involves independent nucleation, propagation, and annihilation of individual domains. Finally, we show that our findings are not at all restricted to Co/Pt multilayers, but are a quite general feature of transitional in-plane to out-of-plane magnetization systems.

DOI: 10.1103/PhysRevB.110.024417

I. INTRODUCTION

Recently, magnetic films with periodic magnetic domain structures, particularly parallel-aligned stripe domains, have garnered renewed interest as reconfigurable magnonic media for high-frequency and low-power consumption devices [1–5], or as basis for neuromorphic reservoir computing [6–8]. To realize such applications, it is crucial to identify magnetic materials that can host aligned stripe domains, while being producible via low-cost fabrication techniques. In this context, magnetic multilayers (MLs) with perpendicular magnetic anisotropy (PMA) are proven to be promising candidates [3–5,9]. However, continuous and parallel aligned stripe domains are usually not the remanent state of the magnetization in magnetic MLs. For example, ML systems with strong PMA can exhibit disordered domain structures, such as labyrinth-, maze-like, or mixed bubble and stripe domain states.

In order to stabilize continuous and almost defect-free parallel magnetic stripe domains without any time-consuming in-plane demagnetization procedure [10–15], it is advantageous to utilize low PMA materials. Such systems with a low Q factor of $Q < 1$ were also studied in the context of rotatable anisotropy [16,17] and weak stripe domain states [18–23]. The Q factor relates the perpendicular magnetic anisotropy energy density in the in-plane (IP) magnetized state K_u to the demagnetization energy density for the out-of-plane (OOP) magnetized state, $1/2\mu_0 M_S^2$, namely, $Q = 2K_u/(\mu_0 M_S^2)$. Besides the PMA, the total ML thickness significantly influences the magnetic ground state, as the demagnetization energy density of a heterogeneous domain state depends on the film thickness [24,25]. By increasing the overall thickness of the ML system with $Q < 1$, the system experiences a magnetization reorientation transition from an IP magnetized ground state to an OOP stripe domain ground state [26–30]. The reorientation occurs through a transient state, which is henceforth referred to as the "tilted magnetization state" [30]. Its magnetic ground state exhibits almost defect-free parallel aligned stripe domains; however, the domain magnetization is not strictly perpendicular, but instead tilted by a certain angle with respect to the surface normal and exhibits a single point of irreversibility in the OOP external magnetic field reversal.

In addition to thin films with $Q < 1$, another class of systems known as hybrid systems consisting of a combination of OOP and IP magnetized layers in a directly exchange-coupled bilayer structure, also may exhibit tilted magnetization behavior [31–34]. This tilting can occur either at the interfaces of the individual layers or across the entire bilayer system if the

*Contact author: p.heinig@hzdr.de

thicknesses of the layers are much smaller than their exchange lengths. In contrast, single layer thin films with $Q < 1$ demonstrate a more uniformly tilted magnetization behavior, even when their thickness exceeds the exchange length.

Despite the extensive research on tilted magnetization stripe domains in the past decades [21,35–42], the in-depth mechanism of their OOP magnetization reversal has not been analyzed and discussed in detail yet. We like to point out that former publications had a different focus on this topic, e.g., the stabilization of high-density bubble domain states at remanence [30]. In contrast, the focus of this paper is the understanding of the unusual combination of an apparent single point of irreversibility in the hysteresis loop paired with a complex remanent stripe domain state, which has so far (even though observed in the past) not been well explained or understood. However, this is crucial, since it has a direct influence on the ability to control the magnetization structure in aligned stripe domains, for example for realizing reconfigurable magnonic media [3]. In this study, we present a comprehensive investigation of the magnetization reversal in fully tunable $[\mathrm{Co}(3.0\ \mathrm{nm})/\mathrm{Pt}(0.6\ \mathrm{nm})]_X$ ML model systems that exhibit a tilted magnetization state. Utilizing vector vibrating sample magnetometry (VSM), magnetic force microscopy (MFM), and micromagnetic simulation, we demonstrate that the magnetization reversal during an OOP external magnetic field sweep in such MLs is dominated by a characteristic distinct irreversible switching point, where mainly the tilted magnetization component transversal to the external field is reversed. Furthermore, we highlight that the direction of the parallel stripe domain state at remanence can be controlled by a small IP magnetic field component. This feature presents a convenient opportunity for spin texture reconfiguration in view of potential applications. In this paper, we refer to the observed magnetic state as the "tilted stripe domain state" rather than a "weak stripe domain state". This terminology choice reflects our focus on the orientation and behavior of stripe domains during the OOP field reversal, rather than on the weak phase contrast observed in Lorentz transmission electron microscopy images, which originally led to the term "weak stripe domains" [43].

II. MATERIALS AND METHODS

To study the magnetic properties in ML systems with stripe domain formation across the magnetization reorientation transition, we prepared $\mathrm{Ta}(1.5\ \mathrm{nm})/\mathrm{Pt}(20\ \mathrm{nm})/[\mathrm{Co}(3.0\ \mathrm{nm})/\mathrm{Pt}(0.6\ \mathrm{nm})]_X/\mathrm{Pt}(2.4\ \mathrm{nm})$ MLs with different Co/Pt bilayer repetition number of $X = 6,\ 11,$ and 22. These three repetition numbers were chosen to investigate different orientation tendencies of the tilted magnetization state from a closer to IP state ($X = 6$) through a transition state ($X = 11$) to a predominant OOP state ($X = 22$) [30]. All samples are grown on Si substrates with a 100-nm-thick thermally oxidized layer (SiO_2) using confocal DC magnetron sputter deposition (ATC 2200 from AJA International Inc.) under an argon atmosphere of 400 mPa at room temperature. Prior to deposition, the chamber base pressure was approximately 2 μPa. To ensure uniform growth of the entire stack, the sample holder was rotated at approximately 1 Hz, and the deposition rate for all materials was maintained below 0.1 nm per second. The Ta layer is used for better adhesion, the 20-nm-thick Pt serves as a buffer layer to promote Co (0001) texture, enhancing vertical coherence throughout the entire multilayer stack [44–47]. The top 3.0-nm Pt layer is used to protect the samples from surface oxidation. For a systematic x-ray reflectometry and x-ray diffraction structural characterization of similar Co/Pt and Co/Au ML sample series from $X = 6$ to $X = 30$ fabricated in the same sputter deposition system with similar parameters, please refer to Refs. [30,48]. We performed magnetometry measurements using a commercial Microsense EZ7 VSM equipped with an electromagnet, which delivers up to 1.85 T magnetic field, and with a $\phi = 360°$ sample rotational stage. Two orthogonal pick-up coil (PUC) pairs are used to record simultaneously the magnetization components parallel (longitudinal) and perpendicular (transversal) to the external field, denoted by m_{LF} resp. m_{TF}, as depicted schematically in Fig. 1(a) as black and blue pair of rings, respectively. Thus, LF and TF denote the components that are longitudinal and transversal to the direction of the external field, respectively. We used a Bruker Dimension Icon magnetic force microscope for magnetic domain imaging. All MFM images were recorded in remanence at room temperature.

When increasing the bilayer repetition number from $X = 6$ via $X = 11$ to $X = 22$, we find that the system undergoes the reorientation transition from an almost typical IP reversal behavior at $X = 6$, as shown in Fig. S1(a) within the Supplemental Material (SM) [49], to an almost typical OOP stripe domain reversal behavior at $X = 22$, see Fig. S1(b) within the SM [49]. The sample with $X = 11$ represents a transitional tilted stripe domain state and exhibits a single point of irreversibility in the OOP field reversal curve as well as a parallel aligned stripe domain state at remanence. Therefore, we will study this sample in more detail as a model system in order to learn more about the characteristics of the tilted stripe domain OOP reversal regime.

We find that each sample has a saturation magnetization M_{S} of 1110 ± 120 kA/m and an effective anisotropy $K_{\mathrm{eff}} \approx -500 \pm 50\ \mathrm{kJ/m^3}$, which corresponds to a uniaxial anisotropy K_{U} of $275 \pm 107\ \mathrm{kJ/m^3}$ and a Q factor of about 0.36 ± 0.14.

III. EXPERIMENTAL RESULTS

Figure 1(b) displays the room-temperature OOP field reversal curves (for both m_{LF} and m_{TF}) of the ML with $X = 11$. Additionally, an inset MFM image at remanence after OOP saturation is included to provide a visual representation of the magnetic domain structure. The OOP field reversal curves for the MLs with $X = 6$ and $X = 22$ at room temperature are shown in Fig. S1 within the SM [49]. Moreover, Fig. S2 within the SM [49] displays the OOP and IP reversal curves for all three samples. The inset MFM image in Fig. 1(b) reveals a clear parallel stripe domain state at remanence with a periodicity of $\lambda = 104$ nm. The field reversal curve in Fig. 1(b) is measured with a magnetic field offset angle $\Delta\phi$ of 1° with respect to the sample surface normal. At high magnetic fields, the TF component is almost zero and gradually increases as the external field is reduced. At a field strength of $H_{\mathrm{TF\,max}}$ [as shown in Fig. 1(b)], the TF component reaches its maximum and then continuously decreases as the field strength decreases. When the magnetic field polarization is

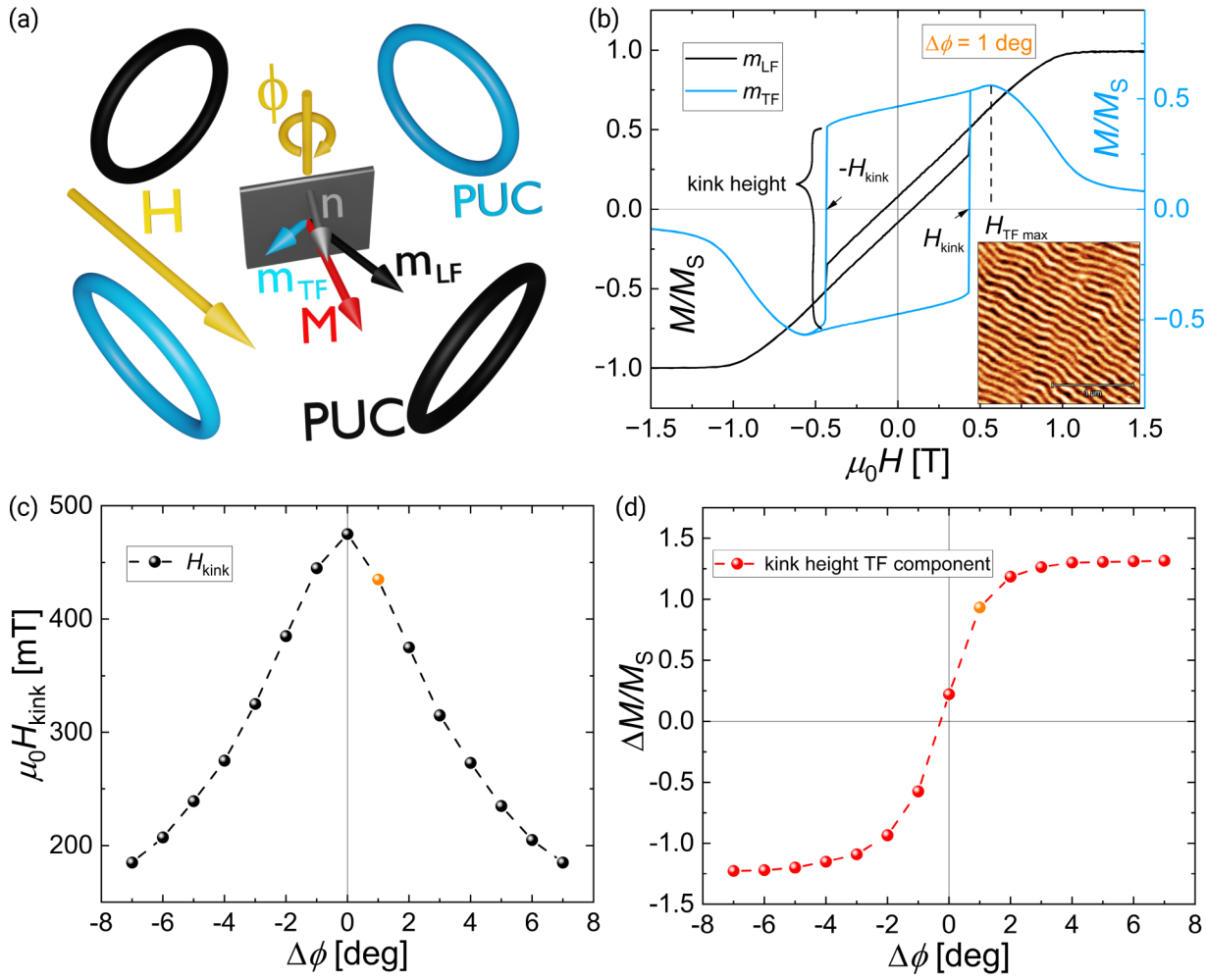

FIG. 1. (a) Schematic representation of the vector-VSM setup. Two pairs of orthogonal pick-up coils (PUC) detect the longitudinal (black PUC) and transversal (blue PUC) components of the sample magnetization (m_{LF} resp. m_{TF}) during an external magnetic field sweep (H). These components are plotted in (b) as functions of the field H. The angle ϕ represents the rotation of the sample surface normal (n) in the plane of the PUCs. The external magnetic field direction is the reference orientation for the rotation angle; hence, $\Delta\phi$ is defined as the angle offset between the sample's normal and the magnetic field. (b) OOP field reversal behavior of the m_{LF} and m_{TF} components for the $[Co(3.0\ nm)/Pt(0.6\ nm)]_{11}$ multilayer system, measured at $\Delta\phi = 1°$. The inserted $2\times2\ \mu m^2$ magnetic force microscopy (MFM) image exhibits the remanent state of the respective sample after positive OOP saturation at 1.85 T. (c) The angular dependence of the kink field H_{kink}, with a highlighted data point representing the hysteresis data from the reversal curve displayed in (b). (d) Angular dependence of the TF component kink height as indicated in (b), again with the $\Delta\phi = 1°$ data point highlighted in orange.

reversed, m_{TF} switches suddenly its direction at the kink field $-H_{kink}$. This switching field ($-H_{kink}$) for the TF component coincides with a sudden point-like step of m_{LF} (and therefore the OOP magnetization component), as can be seen from the OOP magnetization loop [black curve in Fig. 1(b)]. Apart from this in-sync magnetization switching, m_{LF} exhibits a rather linear and reversible behavior during the field reversal process. We note that the kink field value depends on the angle $\Delta\phi$ between the applied external field and the surface normal, as shown in Fig. 1(c). Additionally, the switching height of the TF component [referred to as the kink height in Fig. 1(b)] depends on $\Delta\phi$ as well, as depicted in Fig. 1(d). The m_{LF} and m_{TF} loops corresponding to the data presented in Figs. 1(c) and 1(d) can be found in Fig. S3 within the SM [49]. The angular dependencies of the switching characteristics in Figs. 1(c) and 1(d) are as follows: First, the kink field value is maximal for the (almost) aligned position at $\Delta\phi = 0°$. Conversely, the kink height value is close to zero at this angle. With an increasing deviation from $\Delta\phi = 0°$, the kink field strength decreases, while the absolute kink height increases, eventually reaching a saturation point of around 1.3 at approximately $|\Delta\phi| = 3°$. Additionally, the TF component exhibits a sign inversion when crossing the $|\Delta\phi| = 0$ point in the angular dependence, as shown in Fig. S3 within the SM [49]. A detailed explanation of this behavior is given later along with the discussion of Fig. 6 below. Here, we just note that a higher $\Delta\phi$ causes a larger projection of the external field in the in-plane direction of the sample, which also leads to a better parallel alignment of the domains and domain walls along this IP projection. In the theoretical case of the perfect aligned position $\Delta\phi = 0°$, no IP projection of the external field occurs and hence the domains do not have

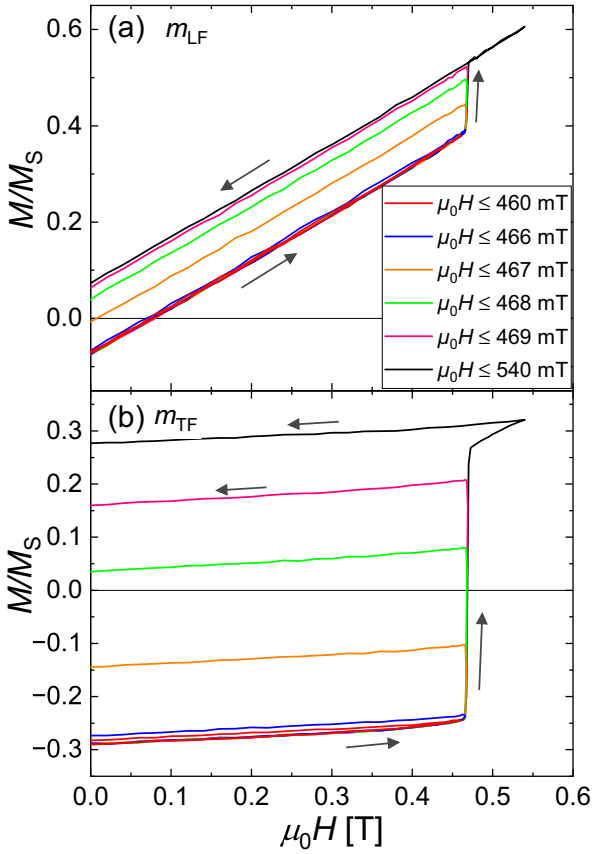

FIG. 2. OOP minor loop series of the $X = 11$ Co/Pt multilayer system at $\Delta\phi = 0(\pm 1)°$ after negative saturation at –1.85 T, (a) component longitudinal to the field and (b) component transversal to the field during an OOP field sweep at room temperature.

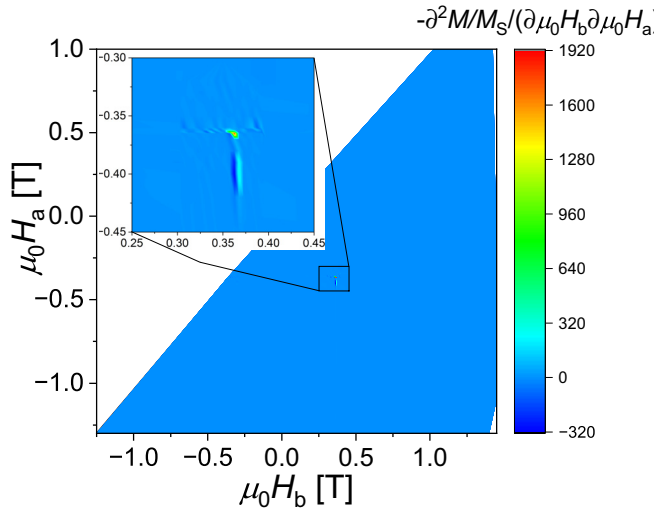

FIG. 3. First-order reversal curve of the [Co(3.0 nm)/Pt(0.6 nm)]$_{11}$ ML at room temperature and at $\Delta\phi = 2(\pm 1)°$ with positive saturation as starting state. The plot shows the negative second derivative of the normalized magnetization over the external return field $\mu_0 H_a$ after positive saturation and the subsequently applied external field $\mu_0 H_b$. Note that this plotting scheme is different from the also often used $\mu_0 H_c$ and $\mu_0 H_u$ plot [$H_c = (H_b - H_a)/2$ and $H_u = (H_b + H_a)/2$]. The displayed data directly exhibit that the whole irreversibility is practically localized at one single point.

a preferred direction to align. Therefore, the stripe domain structure would become random rather than parallel. However, the randomly oriented state is not experimentally observed due to the inevitable small misalignment between the sample surface and the external field in the setup. Hence, we always end up in a parallel stripe domain state after OOP saturation in our experiments.

Once the irreversible switching process at H_{kink} is complete, the system again enters a fully reversible branch. In this branch, the field history no longer affects the macroscopic magnetization versus field behavior any more until the external field reaches the kink field in the opposite direction.

We performed minor loop measurements across the kink to further elucidate the processes occurring during the field reversal, particularly at the kink field H_{kink}. A corresponding minor loop series of the $X = 11$ system is displayed in Fig. 2 for the two magnetization components m_{LF} [Fig. 2(a)] and m_{TF} [Fig. 2(b)]. Each minor loop was measured following the same sequence: beginning with negative saturation at –1.85 T, the measurement commenced at remanence. The external field was then increased to a specific positive field value and subsequently decreased back to remanence. Finally, the system was reset to negative saturation to ensure the exact same starting state for the next minor loop measurement.

The first direct visible information from Fig. 2 is that the single distinct step of irreversibility can actually be resolved into many fine multisteps. They occur within a field range of only 4 mT, so that it is justified to approximate the switching by a single field value, $\mu_0 H_{kink} \approx 468 \pm 2$ mT.

All branches of the minor loops exhibit the same constant slope (as verified by linear fits). Hence, the system behaves completely reversibly at fields different from the kink field and the only irreversibility occurs in the small field range around the kink. This quasi single point occurrence of irreversibility is also well captured by the respective first-order reversal curve (FORC) measurement, as displayed in Fig. 3.

The plotted FORC data in Fig. 3, including the zoomed-in region of interest, clearly shows that for all practical purposes all irreversibility is condensed down to a single point. The vertical negative/positive ridge observed below this point has significantly smaller magnitude compared to the primary irreversible switching behavior. This feature could be attributed to much weaker additional irreversible processes close to the kink field, such as annihilation of remaining isolated bubble domains [29], see also Sec. V.

The stability of the parallel stripe domain state at remanence, combined with the quasi single point irreversibility, suggests that the lateral domain topology remains unperturbed over an extended magnetic field range around remanence. This stability may arise from an intrinsic anisotropy, originating from the IP symmetry-breaking alignment of the stripe domains, which induces an additional energy barrier, thus yielding an easy IP axis along the stripes and a hard IP axis perpendicular to the stripes. Switching the direction of m_{TF}

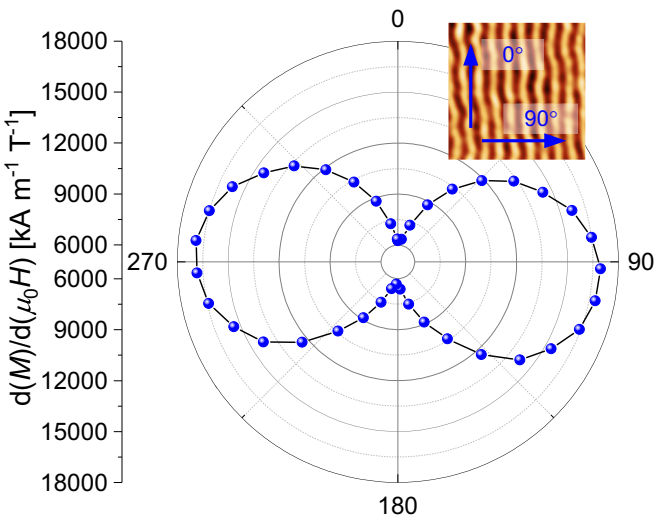

FIG. 4. IP angular ψ dependence of the magnetization slope of the $[Co(3.0\ nm)/Pt(0.6\ nm)]_{11}$ sample (rotated around its surface normal), after OOP saturation, measured with the VSM setup. Slope data measured at room temperature, plotted in polar coordinates, with a schematic illustration of the alignment between stripe domains and external field (at 0° the external field is applied parallel to the stripe domains, at 90° the external field is applied perpendicular to the stripe domains).

requires the Zeeman energy of the IP projection of the external field to overcome this energetic barrier.

The observed angular dependence of the kink field in Fig. 1(c) can be understood based on this induced IP anisotropy. In the case of a perfectly aligned sample geometry, where the external field has a vanishingly small projection within the sample plane, the stripe domains and their domain wall magnetization lack a preferred direction to align and thus require a higher external field to initiate switching. However, with an angle offset $\Delta\phi$, the stripe domains become parallelly aligned, and the TF component together with the external field projection contributes a nonzero IP Zeeman energy term to the total magnetic energy. As a result, the induced anisotropy barrier can be overcome at lower field amplitudes. Increasing the angle offset $\Delta\phi$ leads to a decrease in the required external field for switching.

The effect of the induced anisotropy of the parallel stripe domains can be observed through an IP azimuthal (ψ) angular dependence measurement using the VSM setup, where the sample normal is aligned along the rotation axis. Initially, the $X = 11$ sample is saturated in the OOP direction with a small offset angle of $\Delta\phi = 2°$ to align the stripes consistently in one defined direction at remanence [43,50]. After the stripe domain alignment, the measurement procedure is an IP field sweep within a range of ± 10 mT for various angles ψ between 0 and 180° in approximately 9° increments. The alignment between stripe domains and external field is illustrated in Fig. 4. During the IP field sweep, the magnetization response exhibits a linear behavior without any noticeable hysteresis. The resulting data, which comprises the extracted slope of these linear magnetization responses, is presented in Fig. 4. Because of the symmetry, the data for angles ranging from 180 to 360° is mirrored. Figure 4 showcases the slope data in a polar plot for better visualization.

The observed magnetization behavior reveals distinctive patterns: minimal slopes for the parallel orientation of the magnetic field with respect to the stripe domain long axis ($\psi = 0°$), and maximal slopes for the perpendicular orientation. These findings can be interpreted as follows: In the cases where the external field aligns parallel to the stripe domains, a significant part of the magnetization in the system is already parallel to the external field direction (except for the Néel caps). Consequently, there is limited room for further spins to align in a parallel or antiparallel configuration. This results in minimal changes in magnetization during the external field sweep. Conversely, when the external field aligns perpendicularly with respect to the stripe domains, the magnetization can reversibly tilt in response to the external field. Hence, the angular dependence in Fig. 4 demonstrates the induced anisotropy of the parallel aligned stripe domains. In contrast, when probing the in-plane anisotropy of the system with full IP field reversals we observe an isotropic response with the same in-plane loop for all in-plane directions (see Fig. S4 within the SM [49]). Therefore the observed in-plane anisotropy must be caused by the parallel stripe domain state that is fully maintained during the minor loop analysis of Fig. 4.

IV. MICROMAGNETIC SIMULATIONS

The micromagnetic simulations are performed with the MuMax3 code, a GPU-accelerated simulation program that uses finite-difference discretization in space and time-dependent magnetization dynamics [51]. The specific script here utilized a grid-size implementation of $512\times512\times64$ cells and an overall corresponding sample size of $1024\times1024\times40\,nm^3$ ($x\times y\times z$ coordinate representation), the thickness corresponding to the $X = 11$ experimental system. Periodic boundary conditions with 20 repetitions of the system in x and y directions were set. Additionally, a Voronoi tessellation is implemented into the simulation to define a grain structure with 25-nm-lateral grain size and a normal distribution of the uniaxial anisotropy direction with 99.7% of the randomized directions being within a 10° cone around the OOP direction [52–54] ($3\sigma = 10°$). The magnetic parameters that closely replicate the experimental features are as follows: saturation magnetization $M_S = 1110\,kA/m$, uniaxial anisotropy constant $K_U = 230\,kJ/m^3$, and exchange stiffness $A_{ex} = 11\,pJ/m$. The first two parameters align with the experimental data within the margin of error. The exchange stiffness corroborates well with anticipated values reported in the literature [15,55–58], specifically for the chosen Co thickness in the MLs. Figure S5 within the SM [49] shows the simulated field reversals for different exchange stiffness values in order to obtain the best match with the experimental data. The field reversal data, Fig. 5(a), represents one of nine performed magnetic field-reversal simulations. The nine field-reversal simulations are shown in Fig. S6 within the SM [49]. Each simulation starts with a different initially randomized grain distribution with respective different random number generator seeds. The external field is applied with an offset angle of 3° relative to the surface normal, with the IP field component directed along the positive y direction as

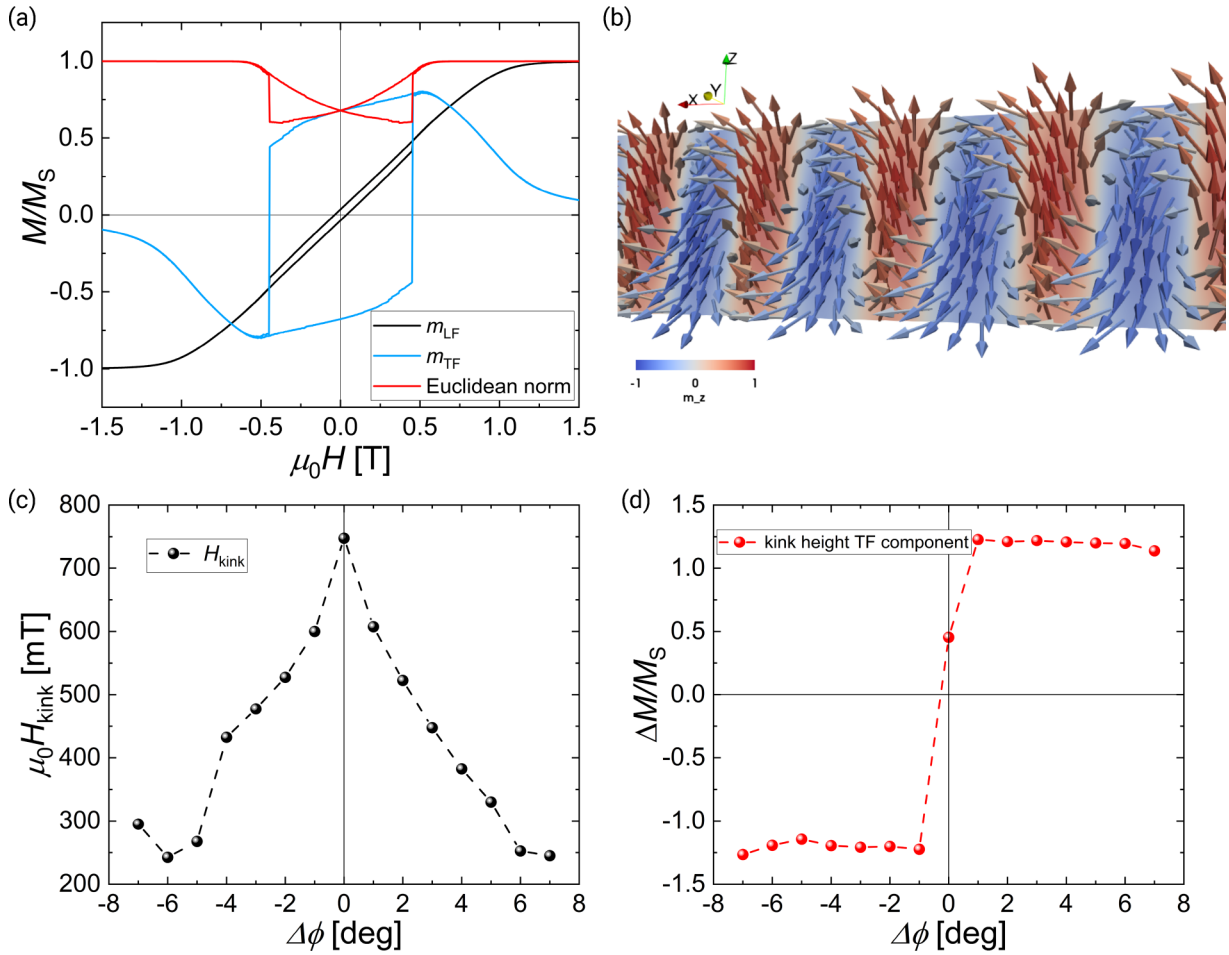

FIG. 5. Micromagnetic MuMax3 simulation data of the respective system with $X = 11$ Co/Pt layer repetitions. (a) Simulation data for one individual simulation showing LF component, TF component and Euclidean norm of both components ($\sqrt{m_{\mathrm{LF}}^2 + m_{\mathrm{TF}}^2}$), at an angle of $\Delta\phi = 3°$. (b) Cross-sectional magnetization illustration of the simulated system in (a) at remanence. The color coding, red and blue, represents 100% of the magnetic moment being aligned in the positive resp. negative z direction. [(c),(d)] Angular dependence of the kink field H_{kink} (c), and the TF component kink height (d), from the simulated system with the same grain distribution as the simulation shown in (c) for different offset angles between surface normal and external field.

well as along the TF component. The field range is between ± 1.9 T. Each of the nine simulations exhibits the same field reversal behavior with slightly different kink field values. In contrast to the experiments, each individual simulation does not show a multistep switching behavior at its respective kink field likely due to the limited sample size considered in the simulation. Consequently, a more detailed investigation of the switching process was not possible in the simulations. Nevertheless, these details lead to the assumption that the switching process starts at a certain grain or grain boundary and is then rather quickly propagating through the whole system. The averaged data of simulated field reversals (shown in Fig. S6 within the SM [49]) exhibits a gradual switching behavior, which can be interpreted as the combined reversal of different areas of a larger system. This would explain the multistep switching behavior of the experimental data, see Fig. 2. However, the width of the kink switching field range for the averaged simulation data is broader than for the experimental data.

Main outcomes of the simulation will be discussed along with Fig. 6 in the following chapter. A novel insight obtained from the simulations is the direct identification of the transition point from homogeneous to heterogeneous tilting and vice versa, observable through the Euclidean norm of the magnetization components, $\sqrt{m_{\mathrm{LF}}^2 + m_{\mathrm{TF}}^2}$. The illustration in Fig. 5(b) captures the simulated remanent magnetization state after OOP saturation. It reveals that all moments within the domains exhibit at least a slight tilt in one IP direction, the positive y direction (of the former IP field component). The magnetization within the domain walls exhibits a nontrivial magnetization structure, consisting of a Néel part at the surfaces and a Bloch component in the bulk.

An additional simulation series is performed for the angle dependence of the systems within a range of $\pm 7°$, similar to the experimental series as shown in Fig. S3 within the SM [49]. The results for the simulations [Figs. 5(c) and 5(d)] are similar to the experimental results, see Figs. 1(c) and 1(d). The kink position agrees rather well with the experiment.

In the literature, simulations were performed with quite similar systems with a low Q factor ($Q < 1$), but not focusing on the OOP field reversal [59–62].

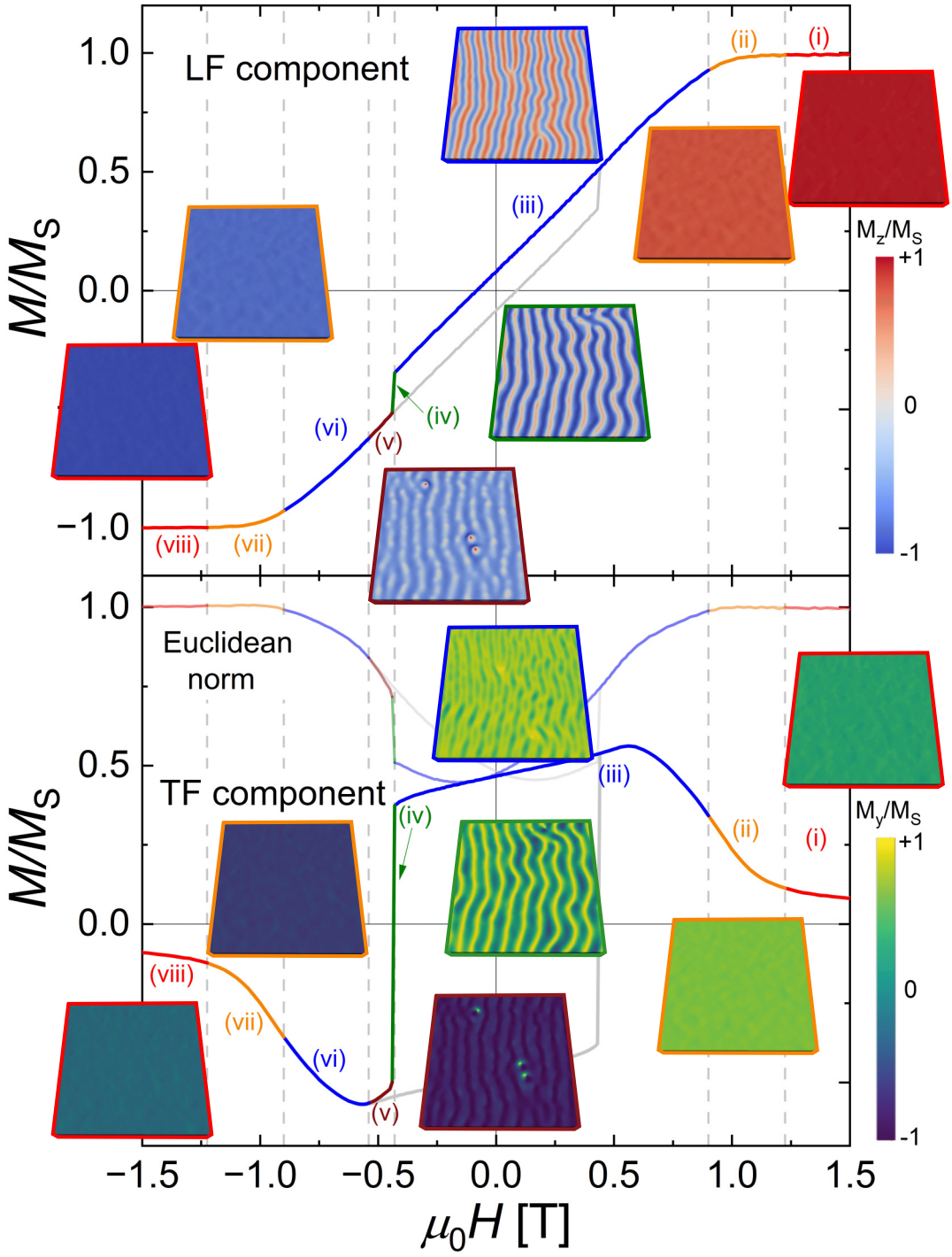

FIG. 6. OOP field reversal of the $X = 11$ sample displayed by LF component (top), TF component (bottom), also including their Euclidean norm, at an angle offset $\Delta\phi = 1°$ [data from Fig. 1(b)], as well as various reversal states (i)–(viii) as obtained from the simulation. Color code legends for the simulated images of the M_z/M_S (top) and M_y/M_S (bottom) components are provided on the right of each plot. Simulated images are assigned to the respective experimental reversal stages in the plots by their matching frame color.

For a detailed analysis of the domain reversal behavior, images were extracted from the simulation, which are presented in the next section. Additionally, three movies of the simulated field reversal for the LF and TF components are included within the SM [49].

V. DISCUSSION

By combining the experimental data with our simulations, we gain a comprehensive understanding of the reversal behavior in our tilted stripe domain system. Figure 6 reviews the experimental hysteresis loop data from Fig. 1, but with

additionally highlighting specific regions of the LF and TF components as obtained in conjunction with the simulations. Additionally, the Euclidean norm of both experimental components and some illustrations of the magnetization alignment and domain structure from the simulated data are displayed. The main difference between the simulated and the experimental Euclidean norm is the field where the Euclidean norm departs from 100%, i.e., where the heterogeneous stripe domain state transitions into a homogeneous uniform state and vice versa. The small discrepancies between the experimental results and simulations highlight the complex nature of the system and the potential influence of additional factors, e.g., reduced exchange coupling at grain boundaries, that are not fully captured in the simulation model yet. As mentioned earlier, LF and TF components denote the magnetization components measured with the two VSM pick-up coils, while in the following OOP and IP components are defined in the usual way with respect to the sample normal. However, both representations differ only slightly due to the small offset angle $\Delta\phi < 10°$.

Starting from positive ("up") OOP saturation, region (i), and reducing the external magnetic field, the simulation data shows that initially when m_{LF} starts decreasing, the magnetization as a whole tilts uniformly towards the IP projection of the external field, region (ii). This homogeneous tilting occurs due to the presence of the small IP field component, i.e., the nonzero $\Delta\phi$, and continues until the field, where the Euclidean norm of m_{LF} and m_{TF} starts decreasing from unity due to the onset of lateral heterogeneity. This constitutes region (iii), where the magnetization fans out into a parallel tilted stripe domain state, with stripes forming along the IP component of the external field, so that the Zeeman energy for the resulting Bloch domain wall IP components is minimized. At the beginning of region (iii), the OOP components of all stripe domains are still parallel to the external field, just with different magnitudes, so the system is in a "more and less" up-oriented stripe domain state. At a lower field $H_{\mathrm{TF\,max}}$, where the maximum in m_{TF} is reached, the magnetization of the "less up" domains crosses the xy plane. Thereafter, the OOP component of these stripe domains is aligned antiparallel to the external field. They then expand in width, whereas the up domains contract in width, while the periodicity of the stripe domains stays constant [11,29]. At remanence, the up and down domain width ratio is nearly one-to-one. The domain walls consist of a Néel part at the surfaces and a Bloch component in the bulk. The overall IP component of the domains and Bloch component of the domain walls remain parallel to the original IP projection of the external field all the way through remanence to H_{kink}.

Passing remanence, both IP and OOP component of the external field reverse sign. This results in the further expansion of the down-oriented domains and a shrinking of the up domains in width, while the stripe domain periodicity again remains constant. The IP projection of the external field is at this point antiparallel to the IP magnetization component of the domains and the Bloch region of the domain walls; hence, this configuration becomes energetically more and more unfavorable for the system as the external field strength increases. Note that the magnetization behavior in regions (i), (ii), and (iii) is completely reversible until the field reaches the kink field value $-H_{\mathrm{kink}}$. There, the IP magnetization component of the domain walls and domains initiates a reversal and switches abruptly into the opposite IP direction due to the increased Zeeman energy being then equal to the energy barrier of the stripe domain induced IP anisotropy (as characterized in Fig. 4). The details of the domain wall switching are still under investigation; however, we assume that the reversal of the Bloch component occurs via the creation of a horizontal Bloch-line through the thickness, which is then propagating along the domain wall, similar as in $Q > 1$ systems [15]. Clusters of domains and domain walls may switch in sync, but then this reversal process may be pinned occasionally in a real sample due to reduced lateral exchange coupling caused by grain boundaries, defects, and other imperfections. As a consequence, we experimentally observe small steps within the kink (see Fig. 2), while our simulations are not able to reproduce such defects and imperfections adequately and do not reveal substeps within the kink even though we implemented an underlying grain structure into our model. However, even in the experiment this field range of pinning amounts to only $\approx$4 mT (less than 1% of H_{kink}), which can be approximated by a single field value, region (iv). Even though we are convinced that the increasing IP Zeeman energy triggers and drives the reversal, also the OOP magnetization component is affected and changes its amplitude, which is seen in the simulation and reveals itself as a distinct and characteristic kink in the LF component of the experimental hysteresis loop. It is important to mention that after the flipping of the IP direction in the domains and domain walls, a few domain walls form isolated bubble domains in the simulation. These localized bubbles then vanish for slightly higher external field values. Thus, these isolated bubbles, if also occurring in the real system, represent an additional small irreversibility of the system. In the experimental data some hints for the isolated bubble occurrence can be found in the field reversal curves, mainly in the TF component of the field reversal for a small field region (v) of $|H_{\mathrm{kink}}| < |H| < |H_{\mathrm{IP\,max}}|$. Notably, the experimentally measured loop shape in region (v) differs slightly when repeating the measurement. Furthermore, this bubble occurrence may be the explanation for the weak vertical negative/positive ridge observed in the FORC diagram of Fig. 3 below the spike-like singularity of the kink field. At the field corresponding to the maximum magnitude of the TF magnetization component $H_{\mathrm{TF\,max}}$, the up domain magnetization crosses the xy plane and this is the ultimate field, where possible remaining isolated bubbles are annihilated.

After the completion of the entire switching process, all domain walls have the same IP magnetization direction again, which is parallel to the small IP projection of the external field. The magnetization behavior in regions (vi), (vii), and (viii) mirrors the exact same behavior observed in regions (iii), (ii), and (i), respectively, but with inverted magnetization profiles. Hence, first the parallel stripe domain state (vi) closes up into a uniformly tilted state (vii) before the system reaches complete saturation (viii). The TF component is not completely zero at the beginning of region (viii), because notably the magnetization is perpendicular to the surface at this point and not parallel to the external field; therefore, the projection of the magnetization into the IP detection coil plane is not completely zero. At even higher fields, the magnetization is

forced to align fully parallel to the external field and not to the surface normal, hence the projection of the magnetization in the IP detection coil plane approaches zero.

In general, the thickness and the related demagnetization energy of this $Q < 1$ system influence the domain width [24] and therefore the domain width to domain wall width ratio [63,64]. Hence, for thicker samples, the ratio is large enough that the system behaves like a regular OOP oriented system [11,29]. The smaller the thickness of the system, the smaller the mentioned ratio becomes. Therefore, the total IP magnetization component becomes stronger and more dominant for the reversal behavior of the system. When the thickness gets too small, the whole system predominantly consists of domain walls so that it becomes an IP oriented system, which was already studied in the past [25]. Between these two regimes, the system under study here represents an interesting intermediate regime, where the OOP stripe domains with large domain wall widths are well alignable along the IP external field component (even if this component is very small in a quasi OOP loop).

The shown and described behavior can become more complex due to different external or internal parameters. Two parameters, that influence the field reversal behavior, are the temperature and the total thickness of the effective magnetic medium, which in our case can be readily tuned by the repetition number X [30,65]. For a thick film, the magnetization in the magnetic medium is dominated by the bulk behavior of the system, where the top and the bottom region are rather independent of each other. In the middle region of the effective medium, the magnetization has enough degrees of freedom to exhibit different magnetic behaviors, e.g. horizontal Bloch-line switching [15]. For thinner magnetic systems the surface effects and magnetization alignment for the flux closing stray fields become more relevant and the bulk behavior gets less dominant for the total energy. For an even thinner system, the surface effects completely dominate the energy landscape of the system and force the magnetization to get more into an IP direction. A similar transition occurs when reducing the temperature, which is driven by the increase of the PMA at low temperatures [66,67]. This can be seen in Figs. S1 and S2 within the SM [49] for the thickness dependence and in Fig. S7 within the SM [49] for the temperature dependence of the $X = 11$ sample magnetic hysteresis. With these two parameters, thickness and temperature, it is possible to tune the system in a way to achieve either one single point of irreversibility (as demonstrated here in this paper) or two extended regions of irreversible switching (dominated by individual independent bubble and stripe domain nucleation, propagation and annihilation with a reversible stripe domain breathing mode around remanence [11]) during the field reversal, such as at temperatures smaller than 100 K (Fig. S7 within the SM [49]), or for the repetition number $X = 22$ (Figs. S1 and S2 within the SM [49]).

A system with a thicker effective magnetic layer than $X = 22$ has an even weaker domain-wall switching behavior of the tilted regime and hence the independent bubble nucleation and annihilation process becomes dominant. An example is a $X = 50$ Co/Pt ML system {loop shown in Fig. S8 within the SM [49]}. In Fig. 7, the respective difference between the upper and lower field-reversal paths of the $X = 11$, $X = 22$, and $X = 50$ systems are plotted. For the tilted regime ($X = 11$), the difference plot exhibits a step function with a plateau between the positive and negative kink field.

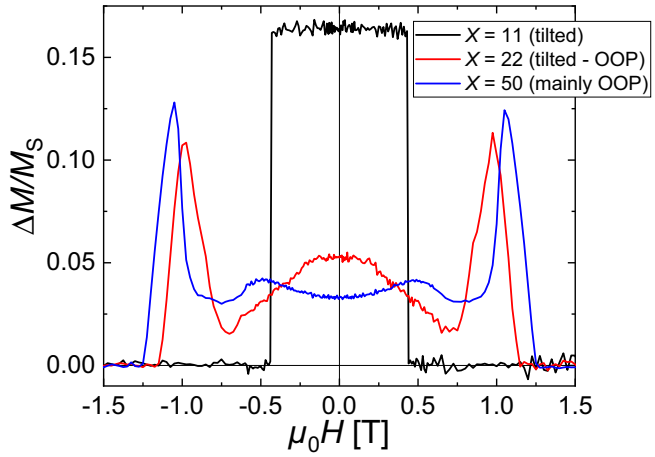

FIG. 7. Difference of the LF component $\Delta M/M_S$ between ascending and descending hysteresis loop branches for $X = 11$, 22 and 50 at $\Delta\phi = 1°$. The graphs display the transition from a single irreversible step behavior ($X = 11$) towards a conventional independent bubble and stripe nucleation, propagation, and annihilation behavior ($X = 50$) [11,12,29].

In case of a pure OOP oriented system, the difference plot would reveal only the two maxima due to the bubble nucleation and annihilation process, with a minimum at zero external field, at which a domain state is present with a nearly complete compensation of the overall magnetization and a low difference between the branches in the breathing mode regime [11]. A system in the transition between tilted magnetization and OOP regime, such as $X = 22$, shows a mixture of these two possible behaviors with the two maxima for the bubble nucleation-annihilation processes as well as the plateau-like behavior around remanence. For thicker systems closer to the OOP regime, such as $X = 50$, the maximum at $\mu_0 H = 0$ T splits up into two local maxima symmetric around the remanent state and a local minimum at remanence.

Our considerations here are of course not limited to Co/Pt ML systems, but are generally valid for any IP to OOP transitional system. In Fig. S9 within the SM [49], two additional examples are shown next to the field-reversal data of the Co/Pt $X = 11$ ML system. Namely, a Fe/Gd ML system {Pt(5 nm)/[Fe(0.35 nm)/Gd(0.50 nm)]$_{80}$/Pt(5 nm)}[68–70] and a single Co layer with a thickness of 29 nm [Ta(1.5 nm)/Pt(20 nm)/Co(29 nm)/Pt(3 nm)] [47]. Additional Lorentz transmission electron microscopy images of the Fe/Gd ML directly demonstrate the crossing of the domain magnetization through the xy plane during the field reversal, see Figs. S10 and S11 within the SM [49].

Besides sample composition, temperature, and thickness, the external field history of the specific sample influences the magnetization alignment, like magnetic stripe domain morphology or bubble density at remanence. The advantage of the tilted magnetization, which is present in the Co/Pt sample with $X = 11$, is that it always exhibits parallel stripe domains at remanence, the alignment of which can be readily tuned by the field history, see Fig. S12 within the SM [49].

In summary, by varying the total thickness (and temperature), the $Q < 1$ ML stripe domain system, as here demonstrated with a $[\mathrm{Co}(3.0\ \mathrm{nm})/\mathrm{Pt}(0.6\ \mathrm{nm})]_X$ system, can be tuned in such a way that only one single point of irreversibility occurs during the field reversal, at a characteristic kink field H_{kink}. Other well-known systems with a similar behavior and just one or two points of irreversibility are the Stoner-Wohlfarth particles [71] or an IP magnetized vortex disk system, but both of them are usually only stabilized in micro- or nanosystems. The tilted magnetization reversal process studied here, on the other hand, occurs in extended macroscale samples as a collective and simultaneous response to an external field. The system's simplicity, as well as the alignability of stripe domains with large wall widths are the two most important results of this study. Based on these findings, further investigations can be performed, e.g., patterning the sample with disk-shaped nanostructures to achieve a mixture of a radial domain structure with a closed IP flux. For specific applications, the system can be adjusted and customized. As a possible application example, the reconfigurability of stripe domains as demonstrated here can be used in electrically contacted bar-shaped nanostructures as the base for a neuromorphic reservoir computing system [7,8], where the input signal is converted into an external field vector to change the magnetic alignment of the domains and domain walls within the bar structure. This would influence the magnetoresistance between the different electrical contacts and could be used as a trainable output signal for reservoir computing.

ACKNOWLEDGMENTS

The authors are grateful to Thomas Naumann and Pierre Pudwell for their experimental and technical support. Additional thanks to Michael Heigl, Aladin Ullrich, and Manfred Albrecht from the Institute of Physics, University of Augsburg, for providing the Fe/Gd multilayer sample and helping with the Lorentz microscopy studies. Finally, we want to thank Ivan Soldatov and Rudolf Schäfer from the IFW, and Jürgen Lindner from HZDR for fruitful discussions and feedback on the manuscript. This work was supported by Deutsche Forschungsgemeinschaft through Project No. 514946929 (Gemischt ferromagnetisch-antiferromagnetische Hybridphase von Streifen- und "Bubble"-Domänenstrukturen für magnonische Kristall und "Race-Track"-Anwendungen) and through TRR 386 A4 (Project No. 514664767).

[1] I. S. Camara, S. Tacchi, L.-C. Garnier, M. Eddrief, F. Fortuna, G. Carlotti, and M. Marangolo, Magnetization dynamics of weak stripe domains in Fe–N thin films: A multitechnique complementary approach, J. Phys.: Condens. Matter **29**, 465803 (2017).

[2] C. Liu, S. Wu, J. Zhang, J. Chen, J. Ding, J. Ma, Y. Zhang, Y. Sun, S. Tu, H. Wang, P. Liu *et al.*, Current-controlled propagation of spin waves in antiparallel, coupled domains, Nat. Nanotechnol. **14**, 691 (2019).

[3] Ch. Banerjee, P. Gruszecki, J. W. Klos, O. Hellwig, M. Krawczyk, and A. Barman, Magnonic band structure in a Co/Pd stripe domain system investigated by Brillouin light scattering and micromagnetic simulations, Phys. Rev. B **96**, 024421 (2017).

[4] P. Gruszecki, C. Banerjee, M. Mruczkiewicz, O. Hellwig, A. Barman, and M. Krawczyk, Chapter Two-The influence of the internal domain wall structure on spin wave band structure in periodic magnetic stripe domain patterns, Solid State Phys. **70**, 79 (2019).

[5] D. Petti, S. Tacchi, and E. Albisetti, Review on magnonics with engineered spin textures, J. Phys. D: Appl. Phys. **55**, 293003 (2022).

[6] G. Bourianoff, D. Pinna, M. Sitte, and K. Everschor-Sitte, Potential implementation of reservoir computing models based on magnetic skyrmions, AIP Adv. **8**, 055602 (2018).

[7] W. Jiang, L. Chen, K. Kaiyuan, L. Li, Q. Fu, Y. Du, and R. H. Liu, Physical reservoir computing using magnetic skyrmion memristor and spin torque nano-oscillator, Appl. Phys. Lett. **115**, 192403 (2019).

[8] K. Nakajima and I. Fischer, *Reservoir Computing: Theory, Physical Implementations, and Applications*, Natural Computing Series (Springer, Singapore, 2021).

[9] R. Salikhov, F. Samad, S. Schneider, D. Pohl, B. Rellinghaus, B. Böhm, R. Ehrler, J. Lindner, N. S. Kiselev, and O. Hellwig, Multilayer metamaterials with ferromagnetic domains separated by antiferromagnetic domain walls, Adv. Electron. Mater. 2400251 (2024).

[10] M. Pardavi-Horvath, J. Oti, G. Vertesy, L. H. Bennett, and L. J. Swartzendrube, A Preisach model study of demagnetized states, J. Magn. Magn. Mater. **104-107**, 313 (1992).

[11] O. Hellwig, G. P. Denbeaux, J. B. Kortright, and E. E. Fullerton, X-ray studies of aligned magnetic stripe domains in perpendicular multilayers, Phys. B: Condens. Matter **336**, 136 (2003).

[12] O. Hellwig, A. Berger, J. B. Kortright, and E. E. Fullerton, Domain structure and magnetization reversal of antiferromagnetically coupled perpendicular anisotropy films, J. Magn. Magn. Mater. **319**, 13 (2007).

[13] M. S. Pierce, J. E. Davies, J. J. Turner, K. Chesnel, E. E. Fullerton, J. Nam, R. Hailstone, S. D. Kevan, J. B. Kortright, Kai Liu, L. B. Sorensen, B. R. York, and O. Hellwig, Influence of structural disorder on magnetic domain formation in perpendicular anisotropy thin films, Phys. Rev. B **87**, 184428 (2013).

[14] M. Hennes, A. Merhe, X. Liu, D. Weder, C. von Korff Schmising, M. Schneider, C. M. Günther, B. Mahieu, G. Malinowski, M. Hehn, D. Lacour, F. Capotondi, E. Pedersoli, I. P. Nikolov, V. Chardonnet, E. Jal, J. Lüning, and B. Vodungbo, Laser-induced ultrafast demagnetization and perpendicular magnetic anisotropy reduction in a Co_{88} Tb_{12} thin film with stripe domains, Phys. Rev. B **102**, 174437 (2020).

[15] R. Salikhov, F. Samad, B. Böhm, S. Schneider, D. Pohl, B. Rellinghaus, A. Ullrich, M. Albrecht, J. Lindner, N. S. Kiselev, and O. Hellwig, Control of stripe-domain-wall magnetization in multilayers featuring perpendicular magnetic anisotropy, Phys. Rev. Appl. **16**, 034016 (2021).

[16] R. J. Spain, Dense-banded domain structure in "rotatable anisotropy" permalloy films, Appl. Phys. Lett. **3**, 208 (1963).
[17] N. Saito, H. Fujiwara, and Y. Sugita, A new type of sagnetic domain structure in negative magnetostriction Ni-Fe films, J. Phys. Soc. Jpn. **19**, 1116 (1964).
[18] G. Ausanio, V. Iannotti, L. Lanotte, M. Carbucicchio, and M. Rateo, Weak stripe domains in Co/Fe multilayers, J. Magn. Magn. Mater. **226-230**, 1740 (2001).
[19] A. Marty, Y. Samson, B. Gilles, M. Belakhovsky, E. Dudzik, H. Dürr, S. S. Dhesi, G. van der Laan, and J. B. Goedkoop, Weak-stripe magnetic domain evolution with an in-plane field in epitaxial FePd thin films: Model versus experimental results, J. Appl. Phys. **87**, 5472 (2000).
[20] F. Virot, L. Favre, R. Hayn, and M. D. Kuz'min, Theory of magnetic domains in uniaxial thin films, J. Phys. D **45**, 405003 (2012).
[21] L.-C. Garnier, M. Marangolo, M. Eddrief, D. Bisero, S. Fin, F. Casoli, M. G. Pini, A. Rettori, and S. Tacchi, Stripe domains reorientation in ferromagnetic films with perpendicular magnetic anisotropy, J. Phys. Mater. **3**, 024001 (2020).
[22] L. M. Álvarez-Prado, Control of dynamics in weak PMA magnets, Magnetochemistry **7**, 43 (2021).
[23] K. Ait Oukaci, D. Stoeffler, M. Hehn, M. Grassi, B. Sarpi, M. Bailleul, Y. Henry, S. Petit, F. Montaigne, R. Belkhou, and D. Lacour, Oscillatory buckling reversal of a weak stripe magnetic texture, Mater. Res. Lett. **11**, 789 (2023).
[24] Z. Malek and V. Kambersky, On the theory of the domain structure of thin films of magnetically uni-axial materials, Czech J. Phys. **8**, 416 (1958).
[25] Y. Murayama, Micromagnetics on stripe domain films. I. Critical cases, J. Phys. Soc. Jpn. **21**, 2253 (1966).
[26] S. Hashimoto, Y. Ochiai, and K. Aso, Perpendicular magnetic anisotropy and magnetostriction of sputtered Co/Pd and Co/Pt multilayered films, J. Appl. Phys. **66**, 4909 (1989).
[27] C.-J. Lin, G. L. Gorman, C. H. Lee, R. F. C. Farrow, E. E. Marinero, H. V. Do, H. Notarys, and C. J. Chien, Magnetic and structural properties of Co/Pt multilayers, J. Magn. Magn. Mater. **93**, 194 (1991).
[28] P. Fischer, T. Eimüller, G. Schütz, M. Köhler, G. Bayreuther, G. Denbeaux, and D. Attwood, Study of in-plane magnetic domains with magnetic transmission x-ray microscopy, J. Appl. Phys. **89**, 7159 (2001).
[29] J. E. Davies, O. Hellwig, E. E. Fullerton, G. Denbeaux, J. B. Kortright, and K. Liu, Magnetization reversal of Co/Pt multilayers: Microscopic origin of high-field magnetic irreversibility, Phys. Rev. B **70**, 224434 (2004).
[30] L. Fallarino, A. Oelschlägel, J. A. Arregi, A. Bashkatov, F. Samad, B. Böhm, K. Chesnel, and O. Hellwig, Control of domain structure and magnetization reversal in thick Co/Pt multilayers, Phys. Rev. B **99**, 024431 (2019).
[31] T. N. A. Nguyen, Y. Fang, V. Fallahi, N. Benatmane, S. M. Mohseni, R. K. Dumas, and J. Åkerman, [Co/Pd]–NiFe exchange springs with tunable magnetization tilt angle, Appl. Phys. Lett. **98**, 172502 (2011).
[32] G. Heldt, M. T. Bryan, G. Hrkac, S. E. Stevenson, R. V. Chopdekar, J. Raabe, T. Thomson, and L. Heyderman, Topologically confined vortex oscillations in hybrid $[Co/Pd]_8$-Permalloy structures, Appl. Phys. Lett. **104**, 182401 (2014).
[33] P. Wohlhüter, M. T. Bryan, P. Warnicke, S. Gliga, S. E. Stevenson, G. Heldt, L. Saharan, A. K. Suszka, C. Moutafis, R. V. Chopdekar, J. Raabe, T. Thomson, G. Hrkac, and L. J. Heyderman, Nanoscale switch for vortex polarization mediated by Bloch core formation in magnetic hybrid systems, Nat. Commun. **6**, 7836 (2015).
[34] L. Fallarino, V. Sluka, B. Kardasz, M. Pinarbasi, A. Berger, and A. D. Kent, Interlayer exchange coupling between layers with perpendicular and easy-plane magnetic anisotropies, Appl. Phys. Lett. **109**, 082401 (2016).
[35] J. M. Alameda, M. C. Contreras, M. Torres, and A. G. Arche, Analysis of magnetization rotational processes in amorphous and crystallized Fe-Si thin films, J. Magn. Magn. Mater. **62**, 215 (1986).
[36] K. M. Krishnan, T. Takeuchi, D. M. Donnet, and K. Tanahashi, Magnetism and magnetization structure of *c*-axis oriented single-crystal cobalt films grown epitaxially on rigid underlayers, J. Appl. Phys. **75**, 7579 (1994).
[37] D. M. Donnet, K. M. Krishnan, and Y. Yajima, Domain structures in epitaxially grown cobalt thin films, J. Phys. D **28**, 1942 (1995).
[38] M. Hehn, S. Padovani, K. Ounadjela, and J. P. Bucher, Nanoscale magnetic domain structures in epitaxial cobalt films, Phys. Rev. B **54**, 3428 (1996).
[39] M. Hehn, K. Ounadjela, R. Ferré, W. Grange, and F. Rousseaux, Reorientational magnetic transition in mesoscopic cobalt dots, Appl. Phys. Lett. **71**, 2833 (1997).
[40] O. de Abril, M. Sánchez, and C. Aroca, The effect of the in-plane demagnetizing field on films with weak perpendicular magnetic anisotropy, J. Appl. Phys. **100**, 063904 (2006).
[41] M. Coïsson, F. Vinai, P. Tiberto, and F. Celegato, Magnetic properties of FeSiB thin films displaying stripe domains, J. Magn. Magn. Mater. **321**, 806 (2009).
[42] P. A. Zezyulina, I. T. Iakubov, A. N. Lagarkov, S. A. Maklakov, S. S. Maklakov, A. S. Naboko, A. V. Osipov, D. A. Petrov, K. N. Rozanov, and I. A. Ryzhikov, Effect of perpendicular anisotropy and eddy currents on the microwave performance of single-layer and multi-layer permalloy films, IEEE Magn. Lett. **7**, 1 (2016).
[43] A. Hubert and R. Schäfer, *Magnetic Domains* (Springer-Verlag, Berlin-Heidelberg, 1998).
[44] W. B. Zeper, H. W. van Kesteren, B. A. J. Jacobs, J. H. M. Spruit, and P. F. Carcia, Hysteresis, microstructure, and magneto-optical recording in Co/Pt and Co/Pd multilayers, J. Appl. Phys. **70**, 2264 (1991).
[45] H. Gong, D. Litvinov, T. J. Klemmer, D. N. Lambeth, and J. K. Howard, Seed layer effects on the magnetoresistive properties of NiFe films, IEEE Trans. Magn. **36**, 2963 (2000).
[46] R. Law, R. Sbiaa, T. Liew, and T. C. Chong, Effects of Ta seed layer and annealing on magnetoresistance in CoFe/Pd-based pseudo-spin-valves with perpendicular anisotropy, Appl. Phys. Lett. **91**, 242504 (2007).
[47] G. Patel, F. Ganss, R. Salikhov, S. Stienen, L. Fallarino, R. Ehrler, R. A. Gallardo, O. Hellwig, K. Lenz, and J. Lindner, Structural and magnetic properties of thin cobalt films with mixed hcp and fcc phases, Phys. Rev. B **108**, 184429 (2023).
[48] L. Fallarino, S. Stienen, R. A. Gallardo, J. A. Arregi, V. Uhlíř, K. Lenz, R. Hübner, A. Oelschlägel, O. Hellwig, and J. Lindner, Higher-order ferromagnetic resonances in out-of-plane saturated Co/Au magnetic multilayers, Phys. Rev. B **102**, 094434 (2020).

[49] See Supplemental Material at http://link.aps.org/supplemental/10.1103/PhysRevB.110.024417 for which provides detailed information on additional Co(3.0 nm)/Pt(0.6 nm) ML samples with $X = 6, 22$ and also 50. Furthermore detailed magnetometry data for different in-plane and out-of-plane offset angles for the X=11 sample are provided as well as respective detailed simulation data including an optimization of the exchange stiffness parameter and grain size distribution. In addition, temperature dependent magnetometry behavior is studied and a comparison to similarly behaving single Co layer and Fe/Gd ML systems is presented. Finally, large scale MFM as well as Lorentz-TEM images are shown that support our concluded reversal model.

[50] M. S. Cohen, Influence of anisotropy dispersion on magnetic properties of Ni–Fe films, J. Appl. Phys. **34**, 1841 (1963).

[51] A. Vansteenkiste, J. Leliaert, M. Dvornik, M. Helsen, F. Garcia-Sanchez, and B. Van Waeyenberge, The design and verification of MuMax3, AIP Adv. **4**, 107133 (2014).

[52] T. Schrefl, J. Fidler, and H. Kronmüller, Remanence and coercivity in isotropic nanocrystalline permanent magnets, Phys. Rev. B **49**, 6100 (1994).

[53] T. Schrefl, J. Fidler, and J. N. Chapman, Micromagnetic modelling of multilayer media, J. Phys. D: Appl. Phys. **29**, 2352 (1996).

[54] R. Salikhov, F. Samad, S. S. P. K. Arekapudi, R. Ehrler, J. Lindner, N. S. Kiselev, and O. Hellwig, Control and tunability of magnetic bubble states in multilayers with strong perpendicular magnetic anisotropy at ambient conditions, Phys. Rev. B **106**, 054404 (2022).

[55] K. D. Belashchenko, Anisotropy of exchange stiffness and its effect on the properties of magnets, J. Magn. Magn. Mater. **270**, 413 (2004).

[56] C. Eyrich, W. Huttema, M. Arora, E. Montoya, F. Rashidi, C. Burrowes, B. Kardasz, E. Girt, B. Heinrich, O. N. Mryasov *et al.*, Exchange stiffness in thin film Co alloys, J. Appl. Phys. **111**, 07C919 (2012).

[57] C. Eyrich, A. Zamani, W. Huttema, M. Arora, D. Harrison, F. Rashidi, D. Broun, B. Heinrich, O. Mryasov, M. Ahlberg, O. Karis, P. E. Jönsson, M. From, X. Zhu, and E. Girt, Effects of substitution on the exchange stiffness and magnetization of Co films, Phys. Rev. B **90**, 235408 (2014).

[58] J.-H. Shim, A. A. Syed, Y. Shin, J.-W. Kim, H.-G. Piao, S.-H. Lee, K. M. Lee, J.-R. Jeong, D.-H. Kim, and D. E. Kim, Ultrafast dynamics of exchange stiffness in Co/Pt multilayer, Commun. Phys. **3**, 74 (2020).

[59] M. Labrune and J. Miltat, Strong stripes as a paradigm of quasi-topological hysteresis, J. Appl. Phys. **75**, 2156 (1994).

[60] M. Labrune and L. Belliard, Stripe domains in multilayers: Micromagnetic simulations, Physica Status Solidi (a) **174**, 483 (1999).

[61] H. Niedoba and M. Labrune, Magnetization reversal via Bloch points nucleation in nanowires and dots: A micromagnetic study, Eur. Phys. J. B **47**, 467 (2005).

[62] O. Zaiets, V. Kravchuk, O. Pylypovskyi, D. Makarov, and D. Sheka, Circular stripe domains and cone state vortices in disk-shaped exchange coupled magnetic heterostructures, J. Phys. D **55**, 445003 (2022).

[63] J. M. D. Coey, *Magnetism and Magnetic Materials* (Cambridge University Press, Cambridge, 2010).

[64] I. Lemesh, F. Büttner, and G. S. Beach, Accurate model of the stripe domain phase of perpendicularly magnetized multilayers, Phys. Rev. B **95**, 174423 (2017).

[65] L. Fallarino, O. Hovorka, and A. Berger, Field orientation dependence of magnetization reversal in thin films with perpendicular magnetic anisotropy, Phys. Rev. B **94**, 064408 (2016).

[66] E. R. Callen and H. B. Callen, Static magnetoelastic coupling in cubic crystals, Phys. Rev. **129**, 578 (1968).

[67] T. Nozaki, M. Oida, T. Ashida, N. Shimomura, and M. Sahashi, Temperature-dependent perpendicular magnetic anisotropy of Co-Pt on Cr_2O_3 antiferromagnetic oxide, Appl. Phys. Lett. **103**, 242418 (2013).

[68] J. Hintermayr, A. Ullrich, and M. Albrecht, Structure and magnetic properties of ferrimagnetic $[Gd/Fe]_n$ multilayer and Gd_xFe_{100-x} thin films, AIP Adv. **11**, 095214 (2021).

[69] N. Y. Schmidt, S. Abdulazhanov, J. Michalička, J. Hintermayr, O. Man, O. Caha, M. Urbánek, and M. Albrecht, Effect of Gd addition on the structural and magnetic properties of L1-FePt alloy thin films, J. Appl. Phys. **132**, 213908 (2022).

[70] R. Hosseinifar, E. Golias, I. Kumberg, Q. Guillet, K. Frischmuth, S. Thakur, M. Fix, M. Albrecht, F. Kronast, and W. Kuch, Influence of magnetic domain walls on all-optical magnetic toggle switching in a ferrimagnetic GdFe film, Beilstein J. Nanotechnol. **13**, 74 (2022).

[71] E. C. Stoner and E. P. Wohlfarth, A mechanism of magnetic hysteresis in heterogeneous alloys, Philos. Trans. R. Soc. London **240**, 599 (1948).